J. Fluid Mech. (1995), *vol.* 287, *pp.* 251–278

Numerical and theoretical solutions for a drop spreading below a free fluid surface

By DOROTHY M. KOCH[1] AND DONALD L. KOCH[2]

[1]Department of Geology and Geophysics, Yale University, New Haven, CT 065120-8109, USA

[2]School of Chemical Engineering, Cornell University, Ithaca, NY 14853, USA

(Received 18 January 1994 and in revised form 7 November 1994)

Numerical solutions are derived for a viscous, buoyant drop spreading below a free fluid surface. The drop has zero interfacial tension, and we consider viscosity contrasts $0.1 < \lambda < 10$ with the surrounding fluid half-space. The density contrast between the drop and outer fluid is assumed to be small compared with the density contrast at the fluid surface. The numerical solutions for the approach and initial spread of the drop below the fluid surface are obtained using the boundary integral method. To facilitate an investigation over a larger range of viscosity contrasts and for longer time periods, we solve for the motion of gravity currents at the fluid surface. For this geometry we also solve the boundary integral equations for the cases $\lambda = 0$ and $1/\lambda = 0$.

For extensive drop spreading, the motion is described by asymptotic solutions. Three asymptotic solutions are derived, which apply for different values of the viscosity contrast relative to the aspect ratio ((radial extent R)/(drop thickness a)). For very low-viscosity drops ($\lambda \ll a/R[\ln(R/a)]^{-1}$), the greatest resistance to spreading occurs at the drop rim, and the asymptotic solution is found using slender body theory. Drops with intermediate viscosity contrast ($a/R \ll \lambda \ll R/a$) are slowed primarily by shear stresses at the lower drop surface, and a lubrication solution (Lister & Kerr 1989) applies. The greatest resistance to the spread of very viscous drops ($\lambda \gg R/a$) comes from the radial stresses within the drop, and the asymptotic solution is independent of the outer fluid. All drops having $0 \ll \lambda \ll \infty$ will eventually spread according to lubrication theory, when their aspect ratio becomes sufficiently large relative to viscosity contrast.

Theoretical results are compared with numerical and experimental results for drops and gravity currents spreading at a fluid surface. The solutions can be applied to aspects of planetary mantle flow where temperature variations cause significant viscosity contrasts. The low-viscosity solution has been applied to study the encounter of a hot, low-viscosity upwelling plume with a planet surface (Koch 1994). Here we apply the high-viscosity asymptotic solution to study how cold downwelling slabs spread at a depth of neutral buoyancy in the Earth's mantle.

1. Introduction

This paper contains a study of the motion of a buoyant drop with arbitrary viscosity contrast as it approaches and spreads below the free surface of a fluid half-space. Large stresses in the fluid layer between the drop and the surface cause the drop to spread laterally just below the surface. We study the approach and initial spreading

Particle	Surface	Study
solid	interface*	Lee & Leal (1982)
solid	interface*;#	Geller, Lee & Leal (1986)
drop*	rigid	Ascoli, Dandy & Leal (1990)
drop#;*	rigid	Pozrikidis (1990*b*)
drop*	interface*	Chi & Leal (1989)
drop*	interface*;rigid	Yiantsios & Davis (1990)
drop#	interface#	Manga *et al.* (1993)

TABLE 1. Previous BIM studies of a drop interacting with a fluid surface or interface. # and * indicate zero and finite interfacial tension respectively.

numerically using the boundary integral method. Asymptotic solutions are obtained for large spreading, which are independent of the initial conditions but depend on the relative values of the viscosity contrast and the aspect ratio of the drop.

We use the boundary integral method (BIM), which allows for high resolution of the motion of thin films, since it permits reduction of the problem to a single one-dimensional integral equation for the motion of the drop surface. A general discussion and review of the boundary integral method as previously applied to problems with free surfaces is provided by Tanzosh, Manga & Stone (1992). Table 1 lists some studies of BIM solutions for a drop or sphere interacting with a surface or interface. In our study, the drop and fluid surface have zero interfacial and surface tension, as is appropriate for the large surfaces of interest in mantle flow applications. Our approach is similar to that of Manga, Stone & O'Connell (1993), except we assume that the upper fluid surface is impenetrable (normal flow is zero), instead of using a deformable upper surface as they do. This assumption is valid if the density contrast between the drop and outer fluid is very small relative to the contrast between the outer fluid and the air above, as is the case for the mantle applications considered here.

One advantage of using the free-slip condition at the fluid surface is that we can formulate the problem using the method of images. The rising drop is mirrored by a sinking drop, thereby satisfying free-slip boundary conditions at the plane of symmetry between the drops (see figure 1). This method eliminates the need to solve for the motion of the upper fluid surface, so that the number of required integral equations is reduced from two to one. As a result we can allow the drops to spread to larger aspect ratios than could be obtained for a deformable surface. We are interested in looking carefully at the physics of drop spreading to see the effects of viscosity contrast, examine how instabilities might occur, and learn whether initial conditions affect long-term drop spreading.

When the drop spreads far enough, the thin film between the drop and the interface may become gravitationally unstable. In addition to this physical instability, it may become difficult for the numerical simulation to describe the thin films. We will argue, however, that the dynamics of drop spreading is relatively insensitive to the thin film. Thus, we will also present numerical simulations of gravity currents adjacent to the interface as a means of determining the long-time spreading of the drops.

Asymptotic solutions are derived which describe spreading when the drop or gravity current's aspect ratio, or radial extent R divided by vertical thickness a, is very large. We will show that there are three different asymptotic spreading behaviours for drops

which have spread thin, depending on the relative values of the viscosity contrast $\lambda = \eta_{\text{drop}}/\eta_{\text{halfspace}}$ and the aspect ratio R/a.

For intermediate values of λ ($a/R \ll \lambda \ll R/a$), the radial component of velocity is nearly uniform across the drop thickness, the thickness tapers off gradually between the central region and the rim, and the flow in the outer fluid is driven primarily by tangential stress at the lower surface of the drop. This behaviour is described using lubrication theory, which approximates the drop motion as that of a thin, buoyant fluid layer with variable thickness (Lister & Kerr 1989).

For very small λ, the greatest resistance to spreading occurs at the rim, so that flow in the surrounding fluid is driven almost entirely by hydrostatic pressure directed radially outward at the rim. The drop has nearly constant thickness $a(r)$, since the fluid in the drop can flow easily in response to pressure gradients which result from variations in thickness thus eliminating these variations. The spreading behaviour is described by slender body theory, and the flow is driven to lowest order by an expanding ring of force at the rim of the drop. We will show that this solution applies for $\lambda \gg a/R[\ln(R/a)]^{-1}$, or for the time limit $t \ll \beta/\lambda^5[\ln(1/\lambda)]^{-5}[\ln(\beta/\lambda^5)]^{-1}$, where $\beta = a^5\eta_1/\Delta\rho g V^2$, $\Delta\rho$ is the density contrast between the drop and outer fluid, V is the volume of the drop, and η_1 is the viscosity of the outer fluid. At larger times, a drop with non-zero λ will approach lubrication theory.

For very high λ, the radial component of velocity in the drop is uniform across the drop thickness. But the viscosity of the drop is large enough that variations of the vertical velocity with depth and radial variations of the horizontal velocity contribute significantly to the stress in the drop and cannot be neglected as they are in lubrication theory. The equations derived in the asymptotic limit $R \gg a$ for very high λ are different from the standard thin film equations. We will show that this solution applies for $\lambda \gg R/a$, or for the time limit $t \ll a^2(\Delta\rho g V/\eta_2)^{-1}$, where η_2 is the viscosity in the drop. When these highly viscous drops spread beyond this limit, they will also make the transition to lubrication theory.

The numerical and theoretical solutions have applications to certain features of planetary convection. The Earth's mantle convects vigorously (Rayleigh number is 10^6–10^8), has infinite Prandtl number (kinematic viscosity/thermal diffusivity), and highly temperature-dependent viscosity. As a result, large temperature (and therefore viscosity) gradients occur across the upwelling and downwelling regions. Upwelling plume heads, or 500–1000 km diameter blobs of hot material which ascend from the boundary layer at the base of the mantle (see figure 12), have viscosities much smaller than the surrounding mantle. The cold downwelling convective limbs, or slabs, are highly viscous. Slabs tend to be tabular: about 100 km thickness and several thousands of kilometres in length. Since the viscosity contrasts are likely to be several orders of magnitude and occur abruptly across the plume and slab surfaces, they are difficult to resolve with large-scale numerical convective models.

Our numerical and theoretical solutions have the advantage of considering large viscosity contrasts, and of resolving the behaviour of the upwelling and downwelling flows when they become very thin. The numerical solutions have been used to model the spread of plume heads beneath the surface of Venus (Koch 1994). In this study, the high-viscosity gravity current theory will be applied to the lateral spreading of slabs after they have sunk to a depth of neutral buoyancy in the mantle. It has been hypothesized (e.g. Machetel & Weber 1991; Tackley *et al.* 1993; Honda *et al.* 1993) that slab material accumulates and spreads at a density discontinuity (at 670 km depth), until a critical mass causes the material to flush into the lower mantle.

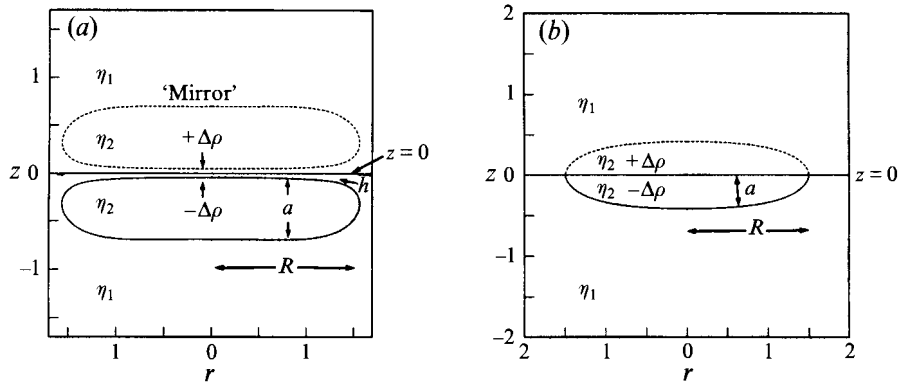

FIGURE 1. Model illustration of (*a*) the drop spreading beneath the fluid surface and (*b*) the gravity current spreading at the surface. The drop and mirror drop (dashed) for the method of images are shown.

We will consider how the high viscosity of the slab reduces the rate of spreading and causes the accumulation to occur more quickly.

Our solutions also have applications to other two-phase flow problems, such as a miscible contaminant rising toward and spreading along a fluid–air interface.

2. The numerical boundary integral solutions

2.1. *Solution technique*

Figure 1 illustrates (*a*) the drop and (*b*) the current geometries and parameters. The drop or current parameters are designated by subscript 2 and the outer fluid by subscript 1. We assume $\rho_1 - \rho_2 \ll \rho_1$ and that the fluid surface $z = 0$ is impenetrable (zero vertical velocity). Figure 1 shows the mirror formulation, in which the flow of the rising buoyant drop or current is superposed on that of a dense sinking mirror drop or current, in order to satisfy the free-slip boundary conditions at $z = 0$.

The governing Stokes equations for flow within the drops and in the surrounding fluid are

$$\nabla p = \eta \nabla^2 \boldsymbol{u} + \rho \boldsymbol{g}; \quad \nabla \cdot \boldsymbol{u} = 0, \tag{2.1}$$

where $\boldsymbol{g}$ is directed vertically downward in the lower fluid and upward in the mirror fluid. We non-dimensionalize lengths using the initial undeformed drop radius R_0, velocities are non-dimensionalized by the drop velocity in an unbounded fluid U_∞, where

$$U_\infty = \frac{1}{3}\frac{R_0^2 g \Delta\rho}{\eta_1}\left(\frac{1+\lambda}{1+\frac{3}{2}\lambda}\right), \tag{2.2}$$

$\Delta\rho = \rho_2 - \rho_1$, $\lambda = \eta_2/\eta_1$, and pressure and stress are non-dimensionalized using $\eta_1 U_\infty / R_0$.

We summarize the procedure for deriving the integral equation and refer to previous studies for further details (e.g. Lee & Leal 1982; Tanzosh *et al.* 1992). Integral equations for the velocity within the drops and the outer fluid, in terms of the velocity and stress along the fluid surfaces, are combined by making use of the condition

$$\boldsymbol{u} \to 0 \text{ as } |\boldsymbol{x}| \to \infty \tag{2.3}$$

and the boundary conditions on the drop interfaces:

$$\boldsymbol{u}_1 = \boldsymbol{u}_2, \tag{2.4}$$

$$\boldsymbol{T}^{(2)} \cdot \boldsymbol{n} - \boldsymbol{T}^{(1)} \cdot \boldsymbol{n} = nz \left[3 \frac{(1 + \frac{3}{2}\lambda)}{(1 + \lambda)} \right] \equiv \boldsymbol{f}, \tag{2.5}$$

where $\boldsymbol{T} \cdot \boldsymbol{n}$ is the stress at the interface and (2.5) contains the (dimensionless) buoyancy driving force. The resulting integral equation for the motion at a point $\boldsymbol{x}$ on the drop interface is:

$$\begin{aligned} \tfrac{1}{2}(\lambda + 1)\boldsymbol{u}(\boldsymbol{x}) = (\lambda - 1) \int_S \boldsymbol{n} \cdot \boldsymbol{K}(\boldsymbol{x} - \boldsymbol{y}) \cdot \boldsymbol{u}(\boldsymbol{y}) \, \mathrm{d}S + \int_S \boldsymbol{J}(\boldsymbol{x} - \boldsymbol{y}) \cdot \boldsymbol{f}(\boldsymbol{y}) \, \mathrm{d}S \\ + (\lambda - 1) \int_{S_m} \boldsymbol{n} \cdot \boldsymbol{K}(\boldsymbol{x} - \boldsymbol{y}) \cdot \boldsymbol{u}(\boldsymbol{y}) \, \mathrm{d}S_m + \int_{S_m} \boldsymbol{J}(\boldsymbol{x} - \boldsymbol{y}) \cdot \boldsymbol{f}(\boldsymbol{y}) \, \mathrm{d}S_m, \end{aligned} \tag{2.6}$$

where $\boldsymbol{J}$ and $\boldsymbol{K}$ are kernels for velocity and stress respectively:

$$\boldsymbol{J} = \frac{1}{8\pi} \left(\frac{\boldsymbol{I}}{|\boldsymbol{r}|} + \frac{\boldsymbol{rr}}{|\boldsymbol{r}|^3} \right), \qquad \boldsymbol{K} = -\frac{3}{4\pi} \frac{\boldsymbol{rrr}}{|\boldsymbol{r}|^5}, \tag{2.7}$$

$\boldsymbol{r} = \boldsymbol{x} - \boldsymbol{y}$, $\boldsymbol{y}$ is on the drop surface S for the lower drop and S_m for the mirror drop, $\boldsymbol{n}$ is the unit outward normal to the drop surface, and the stress difference $\boldsymbol{f}$ is given by (2.5).

The solution procedure is slightly different for the $\lambda = 0$ and $1/\lambda = 0$ gravity current solutions. For $\lambda = 0$, there is no viscous stress and therefore no variation in reduced pressure within the drop. However there is still a non-zero pressure that is independent of position within the drop and is required to prevent volume changes. If we set $\lambda = 0$ in the previous equations we would get zero stress inside the drop, so we modify the normal stress condition (2.5) to include an unknown pressure p_2:

$$\boldsymbol{f} = (3z + p_2)\boldsymbol{n}. \tag{2.8}$$

p_2 is determined by applying the constraint that drop volume remains constant:

$$\int_S \boldsymbol{u} \cdot \boldsymbol{n} \, \mathrm{d}S = 0. \tag{2.9}$$

For a gravity current with a very high viscosity contrast, we can take the limit $\lambda \to \infty$ of (2.4)–(2.7). However, since the motion is independent of the viscosity of the outer fluid, we must now non-dimensionalize all velocities using

$$U_2 = \frac{1}{3} \frac{R_0^2 g \Delta\rho}{\eta_2}. \tag{2.10}$$

Because of the axisymmetry of the drops and currents, analytic integration in the azimuthal direction yields elliptic functions (Lee & Leal 1982) and the surface integrals become one-dimensional integrals. The integrals over the drop and mirror drop are combined by making use of the mirror symmetry between the two drops. The line is discretized using arclength s, and cubic splines are used to express each node point (r, z) as $(r(s), z(s))$. The integrals are performed using a five-point Gaussian quadrature scheme. When observation and integration points $\boldsymbol{x}$ and $\boldsymbol{y}$ coincide, the integrands in (2.6) possess an integrable singularity, which is calculated analytically for a small region close to the singularity. For $\lambda \neq 1$, the velocity in the integrand is assumed to vary linearly between nodes and the solution requires a matrix inversion.

A Langrangian kinematic condition is used to update the drop shape, advancing time by a fixed increment Δt. Our code was developed from code written by Stone for two drops in a biaxial straining flow (see e.g. Stone & Leal 1989 for a related problem).

Having obtained the solution for the velocity at the drop interface, the velocity within the fluid and at the surface of the fluid half-space can be calculated using the equation for the velocity at a point $\boldsymbol{x}$ in the surrounding fluid:

$$\boldsymbol{u}(\boldsymbol{x}) = (\lambda - 1)\int_S \boldsymbol{n}\cdot\boldsymbol{K}(\boldsymbol{x}-\boldsymbol{y})\cdot\boldsymbol{u}(\boldsymbol{y})\,\mathrm{d}S + \int_S \boldsymbol{J}(\boldsymbol{x}-\boldsymbol{y})\cdot\boldsymbol{f}(\boldsymbol{y})\,\mathrm{d}S$$
$$+ (\lambda - 1)\int_{S_m} \boldsymbol{n}\cdot\boldsymbol{K}(\boldsymbol{x}-\boldsymbol{y})\cdot\boldsymbol{u}(\boldsymbol{y})\,\mathrm{d}S_m + \int_{S_m} \boldsymbol{J}(\boldsymbol{x}-\boldsymbol{y})\cdot\boldsymbol{f}(\boldsymbol{y})\,\mathrm{d}S_m. \qquad (2.11)$$

The right-hand side of (2.11) requires $\boldsymbol{u}(\boldsymbol{y})$, the solution (2.6) for the velocity on the drop surface.

The drops were started as spheres at dimensionless depths (depth/initial sphere radius) $d_0 = 5$ or 2. The gravity currents were started as half-spheres (with half the volume of the drops) centred at $r = 0$, $z = 0$. Initially 50 nodes were evenly spaced along the arc length. As the drop or current spreads, additional nodes were added making a total of up to 100 nodes. A smaller node spacing was often employed near the rim in order to resolve the highly curved surface and the relatively high variation in the velocity which occurs there. Enough nodes were used to get a smooth well-defined velocity curve at the rim. The time increment $\Delta t = 0.001$ was used throughout the computations.

To check code accuracy, we compared the initial motion of the spherical BIM drop with analytic results for an instantaneously deformable drop (Koch & Ribe 1989; Koch 1993). For an isoviscous drop, agreement between the BIM numerical and the analytical results is within 0.005% for the velocity (both on the drop and at the fluid surface) and within 0.002% for the pressure at the fluid surface. For $\lambda \neq 1$ we compared the initial BIM drop velocity with that of the series solution for an instantaneously deformable drop. For $\lambda = 10$, there is 0.01% discrepancy, and the $\lambda = 0.1$ drop agrees to 6 significant figures.

In addition, we considered the long-term conservation of drop volume in order to check accuracy at later times. Volume loss is greatest for early spreading and for low-viscosity drops, since shape variations per unit time are greatest in these cases. For example, the greatest volume change per time unit was $\delta V = 0.005$ ($V_0 = 4\pi/3$) for $\lambda = 0.1$ at early times ($t < 15$). Volume change was not a significant problem for the early drop spreading and calculation of surface features required in the plume application (Koch 1994). However, in this study, we are interested in calculating long-time drop spreading rates and these are more sensitive to the accumulated changes in drop volume and shape. Thus, we readjusted the drop surface to keep the volume constant. Further details on code accuracy are desribed in Koch (1993).

2.2. *Numerical results*

2.2.1. *Drop shape and velocity*

The drop shape and spreading behaviour varies with viscosity contrast. Figure 2 shows the cross-sections of two drops having viscosity contrasts $\lambda = 0.1$ and 10 which were started as spheres at $d_0 = 2$ and have spread to radial extent $R = 2$. The lower-viscosity drop curves away from the surface at the rim, with the film and the drop thinnest near the centre axis and with the bottom side concave downward. The concavity increases for larger initial drop depth d_0, since a deeper drop has more time

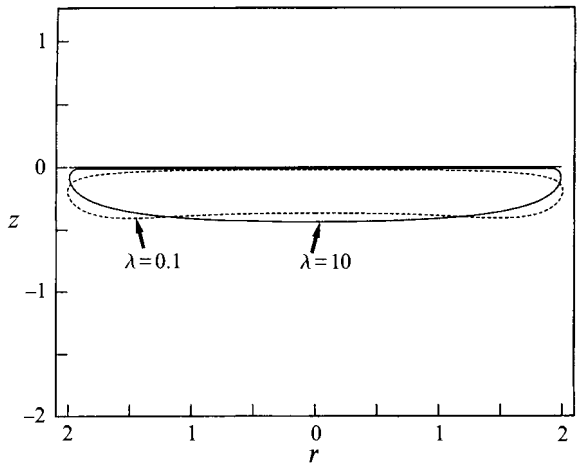

FIGURE 2. Cross-sections of two drops having radial extent $R = 2$: $\lambda = 0.1$ (dashed line), and $\lambda = 10$ (solid line). The fluid surface is the solid line at $z = 0$.

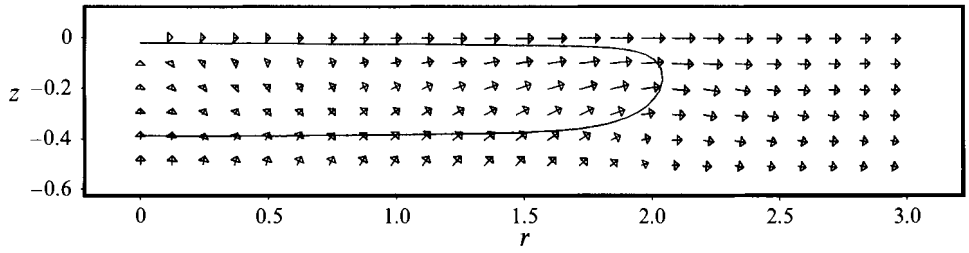

FIGURE 3. Velocity within and around $\lambda = 1$ drop at $R = 2$ (drop shown by solid line). The top row of arrows is the fluid surface $z = 0$.

to deform as it approaches the surface (see figure 6). The high-viscosity drop is more rounded on the side away from the surface and has the thinnest film close to the rim. The film is thinner for the viscous drop, which spreads more slowly giving the film more time to drain.

Figure 3 shows the velocity vectors within and outside an isoviscous drop which was started at $d_0 = 2$ and has spread to $R = 2$. Figure 4 shows the velocity at the surfaces of low (4*a*: $\lambda = 0.1$) and high (4*b*: $\lambda = 10$) viscosity drops which have spread to radial extent $R = 2$. Both drops were started at $d_0 = 2$. (The $\lambda = 10$ drop arrows are scaled 3 times larger than for $\lambda = 0.1$.) The inverse aspect ratio a/R, where a is the drop thickness at $r = 0$, is larger for $\lambda = 0.1$ than for $\lambda = 10$. The change in horizontal velocity across the drop thickness, or $\Delta u = u|_{z=a+h} - u|_{z=h}$ is much larger for the $\lambda = 0.1$ drop since the resistance to internal shearing decreases with λ. The velocity across the low-viscosity drop becomes more uniform as the drop spreads further.

Gravity current shapes are also affected by viscosity contrast. Figure 5 shows the shape of gravity currents which have spread to $R = 3$. The isoviscous current tapers off most gradually from the axis to the current edge, while the $1/\lambda = 0$ and $\lambda = 0$ currents tend to retain a more nearly constant thickness between the axis and rim. The low-viscosity drops and currents have a lip near the rim due to the large resistance of the fluid beyond the rim.

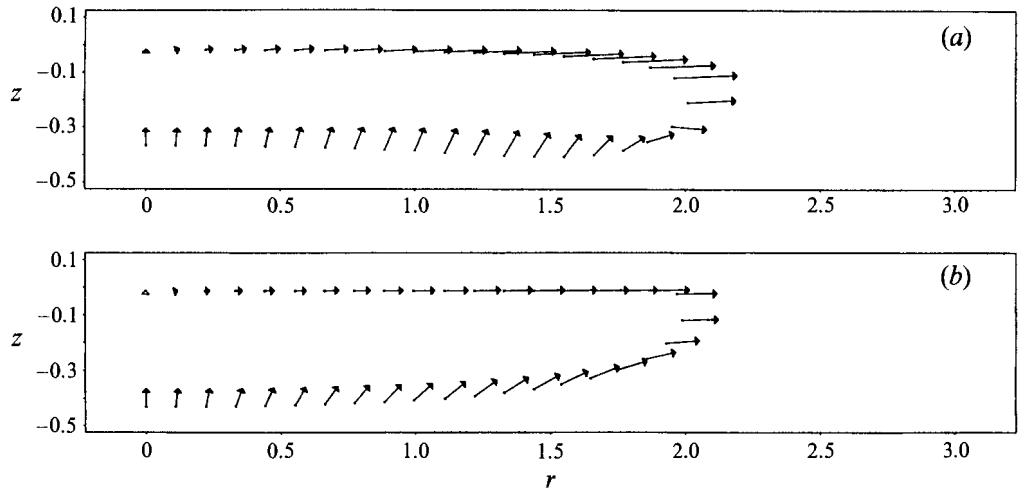

FIGURE 4. (*a*) Velocity at the interface of a $\lambda = 0.1$ drop at $R = 2$. The velocity arrow scaling is twice that used for figure 3. (*b*) Velocity at the interface of a $\lambda = 10$ drop at $R = 2$. The arrow scale is 6 times that used for figure 3.

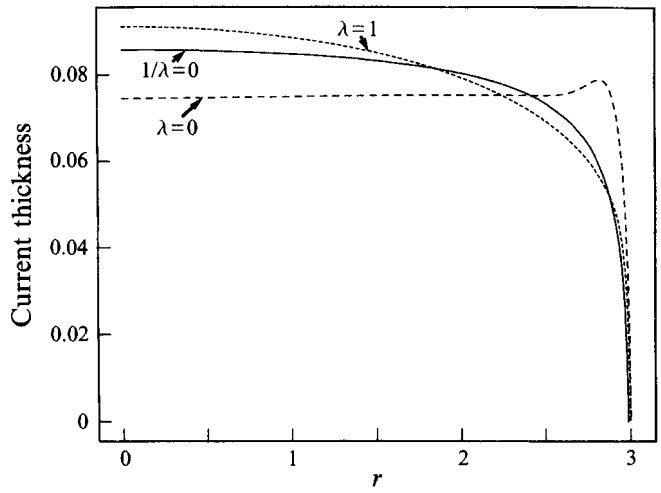

FIGURE 5. Gravity current shapes $a(r)$ at $R = 3$ for $\lambda = 0$, 1 and $1/\lambda = 0$.

The free surface has a significant effect on drop shape, as can be seen by comparing our shapes with those calculated by Pozrikidis (1990*b*) for drops approaching a rigid wall. The no-slip boundary condition at the solid surface creates a greater shear resistance in the film above the drop. The radial velocities on the top and bottom interfaces of a low-viscosity ($\lambda = 0.1$) drop approaching a rigid surface are similar, whereas the velocity on the top interface of a drop approaching a free surface is much larger than that on the bottom where the greatest viscous resistance occurs. Consequently, although Pozrikidis' soft drops curve away from the surface at early times, they do less than in the free surface case. At later times they look more like our larger-viscosity drops, curving toward the surface at the rim. The no-slip boundary condition makes the films near the solid boundary thicker than those near a free surface. For example, $\lambda = 0.1$ drops started at $d_0 = 2$ which have spread to $R \approx 1.8$,

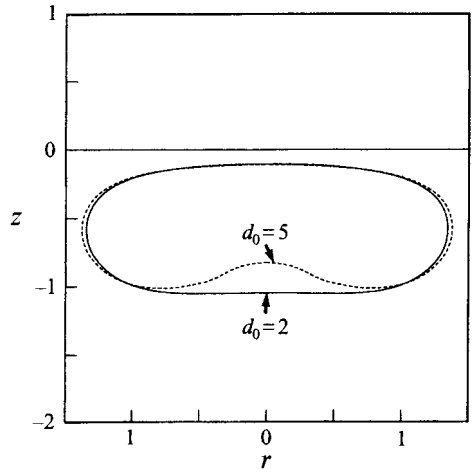

FIGURE 6. Comparison of $\lambda = 0.1$ drops started as spheres at $d_0 = 5$ (dashed line) and $d_0 = 2$ (solid line), after spreading to $R \approx 1.3$.

have a drop-to-film thickness ratio which is $a/h \approx 2$ for a rigid surface and $a/h \approx 15$ for a free surface.

One way to consider the effects of initial conditions on long-term spreading is to vary the initial depth d_0 at which the drops are started as spheres. We compared drop motion and spreading for $d_0 = 2$ and 5 and found that the effect is only significant for early spreading, and is greater for low-viscosity drops. Figure 6 shows two $\lambda = 0.1$ drops with $R \approx 1.3$ which were started at $d_0 = 5$ (dashed line) and $d_0 = 2$ (solid line). The dimpling behaviour, as seen on the lower surface of the $d_0 = 5$ drop, was observed by Pozrikidis (1990*b*) for an isoviscous drop started at distance $d_0 = 8$ from a solid wall. Any perturbation to a spherical drop shape (assuming zero interfacial tension) initiates a hydrodynamic instability in which a slightly oblate spheroid would eventually evolve into a toroid (Kojima, Hinch & Acrivos 1984; Koh & Leal 1989; Pozrikidis 1990*a*). In our calculations an oblate shape is caused by interaction with the fluid surface, but the starting depths are not large enough to lead to significant deformation. In the mantle application, starting depths are about $d_0 = 6$–12, which is also probably too small to form a toroidal shape. Dimples such as the one in figure 6 are damped out by the subsequent spreading and the initial starting depth has little effect on the long-term spreading behaviour. Note that the upper interfaces of the drops in figure 6 are nearly identical. The surface deflection and velocity at the fluid surface $z = 0$ are not greatly effected by d_0.

2.2.2. *Drop and current spreading rates*

We use the numerical solutions to consider the way in which the radial extent and the drop and film thicknesses vary with time for different values of viscosity contrast.

Figure 7 shows the (half) aspect ratio, R/a, as a function of time for both the drops (solid lines) and the gravity currents (dashed lines). Figure 8 shows the variation of radial extent R with time for the drops and currents, as well as for two theoretical solutions which will be derived in § 3. Time is non-dimensionalized here and in the rest of the paper, unless stated otherwise, using

$$t' = t\, R_0 g \Delta\rho / \eta_1, \tag{2.12}$$

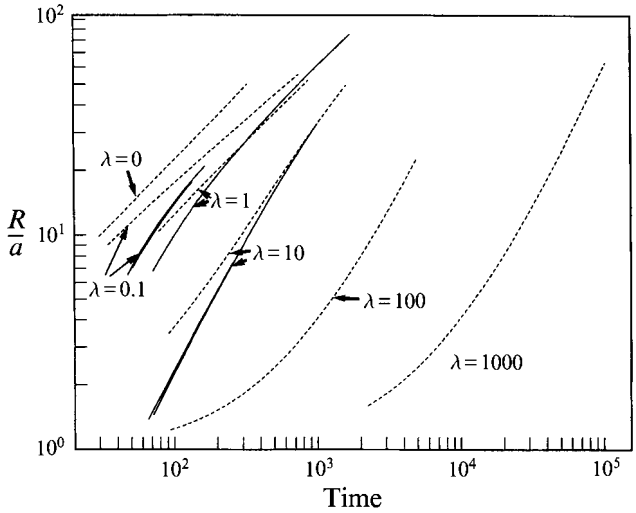

FIGURE 7. Log plot of aspect ratio $R/(a|_{r=0})$ versus t for drops (solid) and gravity currents (dashed). Drops started at $d_0 = 2$ (upper curves for $\lambda = 0.1$ and 10) approach the curves for $d_0 = 5$. Time is increased by $3.0/U_\infty$ for the shallower drops to adjust for the difference in starting depths. Time is non-dimensionalized using $\Delta\rho R_0 g/\eta_1$.

but we omit the prime. The vertical thickness, a, is measured at the centre axis $r = 0$. Starting depths of both $d_0 = 2$ and 5 are shown for $\lambda = 0.1$ and 10. For the shallower drops, we increased the time by $3.0/U_\infty$ and these curves are slightly higher than the curves for the deeper drops but nearly overlap. This suggests that the effect of starting depth on long-term spreading is small. In addition, for each λ, $R(t)$ and $a(t)$ of the drop approach those of the respective gravity current. The mismatch of the isoviscous drop and gravity current at large times is probably due to numerical errors such as long-term volume changes which are greatest for small λ.

Although a power law relation does not necessarily describe the spreading and thinning rates of the current, drop, and film, such a relation is convenient for studying long-term spreading behaviour. So we use the expression:

$$\Gamma = bt^n, \tag{2.13}$$

where Γ is R, a, or h, b is a constant, and we calculate $n \equiv \mathrm{d}(\ln \Gamma)/\mathrm{d}(\ln t)$ numerically. Table 2 shows the values of n for large times (given in the last column). ($R(t)$ for the $\lambda = 1000$ and $\lambda = \infty$ currents are plotted in figure 11 and will be discussed below.)

The constraint that the volume, $V \approx aR^2$, remain constant leads to the prediction that the exponent for thinning should be twice the magnitude of the spreading rate exponent. The deviations from this (see table 2) are due to the fact that a is measured at $r = 0$ and the drops have not yet attained asymptotic shapes. Thus the shapes are nearly, but not exactly, self-similar.

Figure 9 shows that a/h approaches a constant value. The values of a/h for $\lambda = 0.1$ are larger than for $\lambda = 1$ in figure 9 because the low-viscosity drop spreads and thins fastest. For large λ, we can use a scaling argument to predict the variation of a/h with viscosity contrast. The drop will rise as a nearly undeformed sphere until the normal stress in the lubrication gap between the sphere and free surface, which

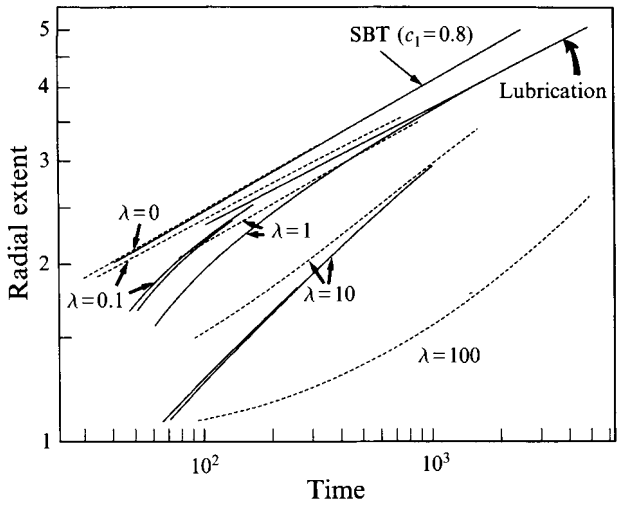

FIGURE 8. Log plot of radial extent R versus t for drops (solid) and currents (dashed). Also shown by solid curves are the slender body solution (using (3.32), with $c_1 = 0.8$) and the lubrication solution (Lister & Kerr 1989), discussed in § 3. R is non-dimensionalized using initial drop radius R_0. Time is non-dimensionalized using $\Delta\rho R_0 g/\eta_1$.

λ	R	a	$\lvert a/R\rvert$	h	t
drops					
0.1	0.28	−0.52	1.9	−0.49	94
1	0.22	−0.43	2.0	−0.47	900
10	0.33	−0.67	2.0	−0.67	650
currents					
0	0.22	−0.45	2.0		190
0.1	0.20	−0.38	1.9		300
1	0.21	−0.42	2.0		870
10	0.30	−0.61	2.0		1100
100	0.38	−0.85	2.2		4800
1000	0.44	−0.94	2.1		100 000
∞	0.46	−0.96	2.1		120*

TABLE 2. Spreading and thinning exponents n for the relation $\Gamma = bt^n$, where Γ is R, a or h. Also shown are the times for which the values n are reported. Time is non-dimensionalized as in (2.12), * except for $\lambda = \infty$ which uses $R_0 g\Delta\rho/\eta_2$.

scales as $\eta_1 Ua/h^2$ (e.g. Yiantsios & Davis 1990), attains the value $\eta_2 U/a$ necessary to deform the drop. This gives the scaling

$$a/h = O(\lambda^{1/2}). \tag{2.14}$$

The values of a/h attained by the deeper drops for $\lambda = 1$, 5 and 10 are $a/h = 11.0$, 22.0, and 32.0 respectively. Therefore, the scaling relation seems to hold for λ as small as 1, and the exact relation is $a/h = 10\ \lambda^{1/2}$.

Figure 9 also shows that the initial drop depth affects the film thickness. The drops started at $d_0 = 2$ have thinner films than the deeper drops with the same λ. Deeper drops are more oblate when they get close to the surface and so are able to trap thicker films.

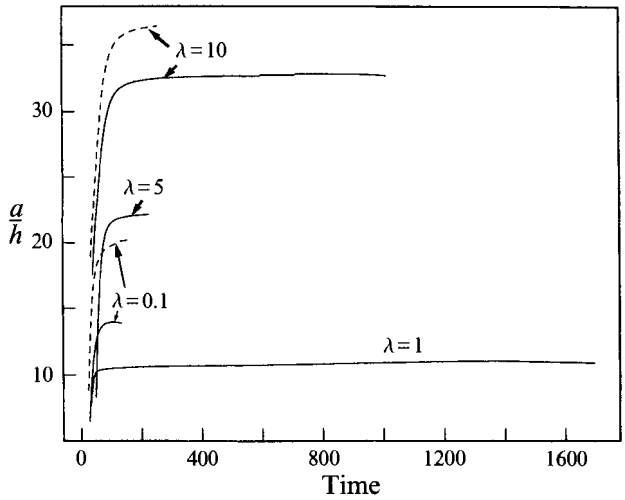

FIGURE 9. Ratio of drop to film thicknesses at $r = 0$ as a function of t. Solid curves are for $d_0 = 5$ and dashed curves for $d_0 = 2$.

Figure 9 and the values of n in table 2 indicate that the film thins at nearly the same rate as the drop. Scaling analysis suggests that the film and drop should thin at the same rate. The film motion due to the ascent of the drop scales as $u = O(\Delta\rho g h a^2/\eta_1 R)$ (Koch 1993). But this velocity is much less than the drop spreading velocity if $\lambda \ll R/a$ (e.g. equations (3.32) and (3.43)), so that the film thins passively above the spreading drop.

Although the film thickness may become as small as the slight deflection of the free surface when h/a is of the same order as $\Delta\rho/\rho$, this is not likely to affect the thinning of the film. The reduced pressure driving the spreading of the drop and film is nearly the same for the deformable and non-deformable free surface as long as the deflection of the deformable surface is much smaller than R.

The relatively dense film between the buoyant drop and the fluid surface is gravitationally unstable. At early times the lateral motion inhibits the growth of gravitational instabilities but, as the drop motion slows, an instability is likely to develop. Numerical instability may also result as the film gets very thin and becomes more difficult to resolve.

The $\lambda = 0.1$ drops broke through the film before the computer calculations were stopped. Instabilities began to develop when the drop spread to about $R = 3$, and when $R = 3.4$ a node near the rim (at $r/R = 0.929$) approached and encountered the surface within one or two time units. Since we believe the instabilities are numerical we show results only up to $R = 3$ in figures 7–9. The $\lambda = 1$ and 10 drops did not become unstable before the computations were stopped, even though the film became quite thin. High drop viscosity thus seems to have a stabilizing effect.

We compare the numerical observations for small λ with experimental observations of drop stability. Griffiths & Campbell (1991) performed experiments for drops beneath a free surface, using glucose syrup and a K_2CO_3 solution ($\lambda \approx 0.003$). Ring shaped instabilities developed in which the film eventually sank through the drop when the drop reached $R \approx 2.2$. The experimental values for n before the onset of instability ($n = 0.22 \pm 0.02$, -0.48 ± 0.03, and -0.5, for R, a, and h, respectively) agree reasonably well with numerical ones for $\lambda = 0.1$ before the nu-

merical instabilities developed. So the experimental and numerical low-viscosity drops have similar spreading behaviour until the development of respective instabilities. Then the experimental drops become unstable as the film sinks through the drop when $R = 2.2$, unlike the numerical drops which seem to break through the film to the surface at larger values of R. The differences in the nature of the instability may be due to the lower values of λ used in the experiments, or to additional instabilities due to molecular effects, or to artificial numerical stability resulting from effects such as axisymmetry, node spacing, or the impenetrable fluid surface.

Linearized Rayleigh–Taylor stability theory for a thin dense film overlying a much deeper layer indicates that the growth rate of the film instability is proportional to film thickness h, and, for a given value of h, the rate increases as λ decreases (Canright 1987; Whitehead & Luther 1975). This is consistent with the numerical results: the $\lambda = 0.1$ drop, which also has the thickest film, breaks through the soonest. The theory predicts that the most unstable wavelength is approximately $5h$–$10h$, depending upon λ. The wide node spacing used in the central portion of the subsurface drops was typically larger than these wavelengths and might therefore tend to inhibit the development of the instability. However, the $\lambda = 0.1$ drop broke through in the central region which had the wider spacing, so it appears that the large node spacing does not preclude the development of the instability.

3. Asymptotic theory for large drop spreading

In §2 we solved numerically the full Stokes flow equations for a drop spreading below and a current spreading along a free fluid surface. These solutions can be obtained with reasonable accuracy up to an aspect ratio R/a of about 20 to 50, depending on the viscosity contrast. For $R \gg a$, the motion is described better using approximate methods. In this section we derive three different asymptotic solutions where each solution corresponds to a different value of the viscosity contrast λ relative to the aspect ratio R/a.

We derive the theories for gravity currents spreading at the fluid surface. For small λ, it appears that a buoyant drop spreading below a denser film eventually becomes gravitationally unstable and breaks through to the fluid surface where it would continue to spread as a gravity current. For $\lambda \geqslant 1$, we argue based on both the scaling and numerical analyses that the film between a drop and a free fluid surface has little effect on the resistance to spreading and therefore the drop spreads like a gravity current. Figures 7 and 8 and the rate exponents given in table 2 show that the drop and current spreading are nearly the same at long times. The scaling arguments are given in detail by Koch (1993) and are summarized here. For $\lambda \ll R^2/ah$, the horizontal velocity in the film is independent of depth and equal to the radial velocity at the upper surface of the drop. This is a consequence of the zero tangential stress condition at the surface $z = 0$. For $\lambda \gg (R/a)^2$, the stress in the film is negligible so that the film does not resist the motion of a very stiff drop. These two conditions overlap, since we observe that $a > h$ in the numerical results. So, if the drop could continue spreading without becoming gravitationally unstable, the asymptotic theory for a drop below the surface would be the same as that for a gravity current.

In §§3.1–3.3 we present scaling analyses for the Stokes flow of gravity currents with $R \gg a$ for different values of λ. We define a reduced pressure so that the term $\rho_1 \boldsymbol{g}$ in the Stokes equations (2.1) is included in the vertical pressure gradient. The surface

of the fluid half-space again has zero tangential stress and vertical velocity. We also make use of a constant volume constraint for the current:

$$V = 2\pi \int_0^R a(r) r \mathrm{d}r. \tag{3.1}$$

In standard lubrication analysis, it is often assumed that the change in horizontal velocity ($\hat{u}(r,z)$) across the fluid film is much larger than the part of the horizontal velocity which does not vary with depth ($U(r)$). This assumption is not necessarily correct for spreading at a free surface. For example, we may compare the change in horizontal velocity which occurs across the drops in figure 4. Figure 4(*a*), the $\lambda = 0.1$ drop, shows a very large variation in horizontal velocity across the drop thickness, so that $\hat{u}(r,z) > U(r)$. But the more-viscous $\lambda = 10$ drop in figure 4(*b*) has $U(r) > \hat{u}(r,z)$. In the scaling analysis we distinguish between these two components of the horizontal velocity, so that

$$u(r,z) = U(r) + \hat{u}(r,z), \tag{3.2}$$

and evaluate the spreading behaviour based on the relative sizes of $\hat{u}$ and U.

3.1. *Low-viscosity drops: slender body theory*

For sufficiently small λ, we can assume that there are large variations of horizontal velocity with depth in the current and use the scaling

$$\frac{\hat{u}_2}{a^2} \gg \frac{U_2}{R^2}, \tag{3.3}$$

so that the r-component of the equation of motion scales as

$$\partial_r p_2 = O\left(\eta_2 \frac{\hat{u}_2}{a^2}\right), \tag{3.4}$$

where the subscript 2 refers to the current. The scaling for continuity is then

$$\frac{(U_2, \hat{u}_2)}{R} = O\left(\frac{w_2}{a}\right), \tag{3.5}$$

where $(U_2, \hat{u}_2)$ indicates the larger part of U_2 and $\hat{u}_2$. Combining (3.3)–(3.5) gives the result

$$p_2 = O\left(\eta_2 R \frac{\hat{u}_2}{a^2}\right) \gg O\left(\eta_2 \frac{(U_2, \hat{u}_2)}{R}\right) = O\left(\eta_2 \frac{w_2}{a}\right). \tag{3.6}$$

Using (3.6), the scaling for the z-component of the equation of motion is

$$\frac{p_2}{a} = O(\Delta\rho g). \tag{3.7}$$

Substitution of (3.7) into (3.4) gives:

$$\hat{u}_2 = O\left(a^2 \partial_r a \frac{\Delta\rho g}{\eta_2}\right), \tag{3.8}$$

where we have retained the r-derivative so that we can find a scaling for the way the thickness varies with r.

We will say that a current has a 'rim' if its thickness near the edge $a(r_e)$, where $a \ll R - r_e \ll R$, is the same order of magnitude as the thickness near the axis $a(r = 0)$. It will be shown that very low-viscosity drops form a rim and this rim drives much of the fluid motion. The velocity solution for Stokes flow close to a two-dimensional

source of motion, in this case the flow in the outer fluid near the edge of a thin laterally spreading current which has a rim, has the scaling (Batchelor 1970)

$$u_o = \frac{\sigma_{rr} a}{\eta_1} \ln\left(\frac{R}{a}\right), \tag{3.9}$$

where the subscript 'o' refers to the outer fluid (at $r > R$) and σ_{rr} is the normal stress at the drop rim. The scaling for the normal stress at the rim is given by the hydrostatic pressure as shown in (3.6) and (3.7). Combining this with (3.9), we get

$$u_o = O\left(\frac{\Delta\rho g a^2}{\eta_1} \ln\left(\frac{R}{a}\right)\right). \tag{3.10}$$

The force exerted by the current rim on the outer fluid is found by integrating the stress over the area of the rim, which has the scaling

$$F_r = O(2\pi a R \sigma_{rr}) = O\left(2\pi\Delta\rho g a^2 R\right). \tag{3.11}$$

The scaling for the tangential stress matching condition on the lower surface of the current is

$$\eta_2 \frac{\hat{u}_2}{a} = O\left(\eta_1 \frac{u_\ell}{R}\right), \tag{3.12}$$

where the subscript ℓ refers to the fluid below the current, and R is the length scale appropriate for fluid flow variations there. Higher-order terms which would appear because the lower surface is not horizontal can be neglected.

Using (3.12) and (3.8), the stress in the lower fluid has the scaling

$$\sigma_\ell = O(p_\ell) = O\left(\eta_1 \frac{u_\ell}{R}\right) = O(\Delta\rho a \partial_r a). \tag{3.13}$$

The force exerted on the lower fluid is found by integrating the stress over the lower surface of the drop, which has the scaling

$$F_\ell = O(\pi\Delta\rho g R^2 a \partial_r a). \tag{3.14}$$

Now we consider the drop shape in order to scale the change of a with r so that we can compare the forces on the rim (3.11) and lower surface (3.14). We define the change in drop thickness with r to be

$$\Delta a = a(r = 0) - a(r_e).$$

Combining this with (3.8) gives the result

$$\Delta a = O\left(\frac{\eta_2}{\Delta\rho g} \frac{R}{a^2} \hat{u}_2\right). \tag{3.15}$$

Matching $\hat{u}_2$ within the drop where drop thickness $a = O(a(r = 0))$, with u_o evaluated at $r = R$ using (3.10), we obtain

$$\frac{\Delta a}{a(0)} = O\left(\lambda \frac{a(r_e)^2}{a(0)^2} \frac{R}{a(0)} \ln\left(\frac{R}{a(r_e)}\right)\right). \tag{3.16}$$

For sufficiently small λ, we expect that any pressure gradients which result from variations in drop thickness will be eliminated by the relatively fast flow within the drop, so that Δa is very small or $a(0) \approx a(r_e)$ and (3.16) becomes

$$\frac{\Delta a}{a} = O\left(\lambda \frac{R}{a} \ln\left(\frac{R}{a}\right)\right). \tag{3.17}$$

This shows that $\Delta a \ll a$ for $\lambda \ll a/R[\ln(R/a)]^{-1}$, which is the condition for constant drop thickness with r, or a 'disk-shaped' drop.

Now we look at the balance between the forces at the rim and at the lower surface of the drop. For the disk-shaped drop, $\Delta a \ll a$, we use (3.17), (3.14) and (3.11) to get the ratio of the force on the rim to that on the lower surface:

$$\frac{F_r}{F_\ell} = O\left(\frac{2}{\lambda}\frac{a}{R}\left[\ln\left(\frac{R}{a}\right)\right]^{-1}\right). \tag{3.18}$$

If $\lambda \ll a/R[\ln(R/a)]^{-1}$, the force at the rim is larger than that on the lower surface. An asymptotic scaling could be derived for $a/R[\ln(R/a)]^{-1} \ll \lambda \ll a/R$ in which $a(r_e) \neq a(0)$ but the rim still has a large effect on the spreading rate. However, we do not pursue this solution since it is applicable to such a restricted parameter regime. It is also possible that a current which has not reached a self-similar disk shape will still have a rim but with $\Delta a = O(a)$. Then the ratio of the force at the rim to that on the lower surface, using (3.11) and (3.14), is

$$\frac{F_r}{F_\ell} = O(1), \tag{3.19}$$

but the spreading induced by the rim is still logarithmically greater than that induced by the lower surface.

We can show that the pressure exerted by the lower fluid on the drop is negligible. The ratio of the pressure within the drop to that below, using (3.4), (3.12) and (3.13), is

$$\frac{p_2}{p_\ell} = O\left(\lambda\frac{R^2}{a^2}\frac{\hat{u}_2}{u_\ell}\right) = O\left(\frac{R}{a}\right) \gg 1. \tag{3.20}$$

We have shown that a drop with $\lambda \ll a/R[\ln(R/a)]^{-1}$ is disk shaped and has the largest force at the rim. Since the spreading motion is limited by the resistance of the fluid beyond the rim, the drop spreading velocity is given by (3.10). To solve for the dependence of R on time, we substitute the volume conservation (3.1) scaling ($V = O(aR^2)$) into (3.10) to get

$$\frac{\mathrm{d}R}{\mathrm{d}t} \equiv u = O\left(\frac{\Delta\rho g V^2}{\eta_1 R^4}\ln\left(\frac{R^3}{V}\right)\right). \tag{3.21}$$

The integration of (3.21) gives

$$R = O\left(\frac{\Delta\rho g V^2}{\eta_1}\, t\ln\left(\frac{\Delta\rho g R_0 t}{\eta_1}\right)\right)^{1/5}, \tag{3.22}$$

so that the relation between R and t is $R \sim [t\ln t]^{1/5}$. The upper time limit for which slender body theory applies is found by combining $\lambda \ll a/R[\ln(R/a)]^{-1}$ and (3.22). For times larger than $t \ll \beta/\lambda^5[\ln(1/\lambda)]^{-5}[\ln(\beta/\lambda^5)]^{-1}$, where $\beta = a^5\eta_1/\Delta\rho g V^2$, a low-viscosity current will begin to approach lubrication theory.

Now we seek a quantitative solution for the spreading of the low-viscosity drop. Because the driving force is given approximately by a line distribution of forces (the buoyancy stress or pressure directed radially outward at the rim), an asymptotic solution will be found using slender body theory. Slender body theory is generally used to solve for the motion of a body with high aspect ratio moving in a viscous fluid, such that the fluid velocity outside the body is driven approximately by a line distribution of forces. For example, Batchelor (1970) used this theory to approximate

the motion caused by a rod translating in a viscous fluid, by solving for the appropriate line distribution of 'Stokeslets' that satisfies the boundary conditions on the rod. A Stokeslet is a singular solution of the Stokes flow equations representing the effect of a point force applied to a fluid. For our problem, we assume that the motion outside the drop can be obtained by integrating over a ring of radially directed normal force Stokeslets which drive the flow at the drop rim. This lowest-order outer solution is independent of the exact shape of the drop surface or the boundary conditions at the drop surface (Batchelor 1970).

We define coordinates in the outer fluid so that

$$\boldsymbol{r}_o = (\tilde{r}_o, \theta, z_o) = (\tilde{r}/R, \theta, z/R), \tag{3.23}$$

where $\tilde{r}$ is the radial component. The general form for the velocity at some point in the outer fluid is given by (2.11), where $\boldsymbol{r} = \boldsymbol{r}_o$. Again we make use of the method of images. To simplify the presentation, we will consider only the radial velocity u at $z = 0$, although the derivation could be generalized to consider other positions and both velocity components. In the asymptotic limit, (2.11) can be simplified using the following. (i) The flow is driven primarily by the normal stress at the rim, which is given approximately by $\sigma_{rr} \approx -p$. (ii) The first and third terms on the right-hand side of (2.11) can be neglected, since they have the scaling $O(ua/R)$ near the rim which is $O(a/R)$ smaller than the left-hand side. (iii) $\boldsymbol{J}$ has a relatively small variation with z. (iv) The integrals over S and S_m are combined using $u(a) = u(-a)$, $\sigma_{rr}(a) = \sigma_{rr}(-a)$ and $e_r(a) = e_r(-a)$. Applying (i)–(iv) to (2.11), the radial velocity at $z = 0$ is given by

$$u(\boldsymbol{r}_o) = \frac{R}{4\pi\eta_1} \int_0^{2\pi} \mathrm{d}\theta'\, \boldsymbol{e}_r \cdot \left[\frac{\boldsymbol{I}}{|\boldsymbol{r}|} + \frac{\boldsymbol{rr}}{|\boldsymbol{r}|^3}\right] \cdot \boldsymbol{e}_{r'} \int_0^a p\, \mathrm{d}z', \tag{3.24}$$

where primes indicate integration variables. Using $p = 0$ at the bottom of the drop ($z = a$), as justified by (3.20), we integrate the pressure to get

$$\int_0^a p\, \mathrm{d}z' = -\int_0^a \Delta\rho g(z' - a)\, \mathrm{d}z' = \tfrac{1}{2}\Delta\rho g a^2. \tag{3.25}$$

Using (3.25), (3.24) can be written

$$u(\boldsymbol{r}_o) = \frac{\Delta\rho g a^2}{8\pi\eta_1} \int_0^{2\pi} \left[\frac{\boldsymbol{e}_r \cdot \boldsymbol{e}_{r'}}{|\boldsymbol{r}|} + \frac{(\boldsymbol{e}_{r'} \cdot \boldsymbol{r})(\boldsymbol{e}_r \cdot \boldsymbol{r})}{|\boldsymbol{r}|^3}\right] \mathrm{d}\theta'. \tag{3.26}$$

This can be rewritten (see e.g. Davis, Schonberg & Rallison 1989)

$$u = \frac{\Delta\rho g a^2}{4\pi\eta_1} \frac{1}{(\tilde{r}_o^2 + 1)^{1/2}} \int_0^{\pi} \frac{\cos\theta\, \mathrm{d}\theta}{(1 - k^2 \cos\theta)^{1/2}} \tag{3.27}$$

where $k^2 = 2\tilde{r}_o/(\tilde{r}_o^2 + 1)$.

In order to evaluate the velocity at the drop surface, the outer coordinate is allowed to approach the drop surface, $\tilde{r}_o \to 1$, in (3.27). The integral is expressed in terms of elliptic integrals so that

$$I \equiv \int_0^{2\pi} \frac{\cos\theta\, \mathrm{d}\theta}{(1 - k^2 \cos\theta)^{1/2}} = \frac{4}{2^{1/2}}[\mathbf{K}(k) - 2\mathbf{E}(k)], \tag{3.28}$$

where $\mathbf{K}$ and $\mathbf{E}$ are elliptic integrals of the first and second kind respectively. In the

limit of $\tilde{r}_o \to 1$, $k \to 1$, the elliptic integrals are singular and can be evaluated using series expansions (see e.g. Lee & Leal 1982), with the result

$$I = \frac{4}{2^{1/2}}\left[\ln\left(\frac{4}{(1-k^2)^{1/2}}\right) - 2 + O((1-k^2)\ln(1-k^2))\right]. \tag{3.29}$$

In order to take the limit, use the expansions:

$$\tilde{r}_o = 1 + x(a/R) \equiv 1 + x\epsilon, \qquad k^2 \approx 1 - \tfrac{1}{2}x^2\epsilon^2, \tag{3.30}$$

where x is the 'inner' coordinate which is defined to be zero at the drop interface. Substituting (3.30), (3.29) and (3.28) into (3.27), we obtain the result

$$u = \frac{\Delta\rho g a^2}{4\pi\eta_1}\left[\ln\frac{4(2)^{1/2}R}{a} - 2 - \ln x\right]. \tag{3.31}$$

The $\ln x$ term is used to match to the inner solution.

For leading-order matching, the inner solution will contain a $\ln x$ term, whose magnitude is determined by the net force per unit length exerted by the drop rim, and a constant velocity term which is approximately equal to $\mathrm{d}R/\mathrm{d}t$. These terms can be matched to the first and third terms on the right-hand side of (3.31). The result gives us the velocity solution

$$\frac{\mathrm{d}R}{\mathrm{d}t} = \frac{\Delta\rho g a^2}{4\pi\eta_1}\left[\ln\frac{4(2)^{1/2}R}{a} + c_1\right], \tag{3.32}$$

where c_1 is a constant having $O(1)$. To solve for the dependence of R on time, we set $c_1 = 0$ in (3.32), use the volume relation $a \approx V/(\pi R^2)$, and integrate (3.32) to get

$$R = [Bt\ln(t/q)]^{1/5}, \tag{3.33}$$

where $B = 3\Delta\rho g V^2/(4\eta_1\pi^3)$ and $q = \eta_1/(\Delta\rho g R_0)[V/(4(2)^{1/2}\pi R_0^3)]^{5/3}$. To obtain the next higher-order correction to (3.32), which is only $O([\ln R/a]^{-1})$ smaller, one would have to match (3.31) to an inner solution determined by solving for the flow and detailed interface shape near the rim. These higher-order terms are significant even for fairly large aspect ratio.

We may use the numerical solution for $\lambda = 0$ to solve for c_1 in (3.32). Comparison of (3.32) with the derivative of the numerical solution indicates that c_1 is approximately 0.8. The slender body theory (SBT) theory solution plotted in figure 8 is found by using $c_1 = 0.8$ and integrating (3.32) numerically. Table 2 indicates that the spreading rate exponent in (2.13) has the value $n = 0.22$ for $\lambda = 0$. If instead of (2.13), we take the derivative $\mathrm{d}R/\mathrm{d}(t\ln t)$, the exponent is 0.19 and appears to be rising and converging to 1/5 at the end of the computation, consistent with (3.33). We will discuss the SBT solution further in the following section where we compare it with the lubrication solution. The $\lambda = 0.1$ drops have $a/R = 0.1$ when $R = 2$ and therefore have λ too large to qualify for the SBT asymptotic solution.

3.2. *Intermediate-viscosity drops: lubrication theory*

For larger λ, the radial velocity in the drop has small variations across the current thickness, so that $U_2 \gg \hat{u}_2$. The spreading is resisted by shear stress from the fluid below the drop, which is evenly distributed along the drop–lower fluid interface. This causes the drop shape to taper gradually to zero with r, rather than having a blocky shape and a thick rim as for low λ (compare current shapes in figure 5 for $\lambda = 0$ and 1). Equations (3.3)–(3.9) continue to apply, but for this case the drop spreading

velocity is determined by matching to the lower fluid, using the stress condition (3.12). The velocity boundary condition on the lower surface of the current is $u_\ell = O(U_2)$. Substituting this into (3.12) gives the tangential stress relation:

$$U_2 = O(\hat{u}_2 \lambda R/a), \tag{3.34}$$

so that the condition for $U_2 \gg \hat{u}_2$ is $\lambda \gg a/R$.

Substituting (3.34) into (3.8), and using $\Delta a = O(a)$ and (3.1), we obtain the scaling for the spreading velocity:

$$u \equiv \frac{\mathrm{d}R}{\mathrm{d}t} = O\left(\frac{\Delta\rho g a^2}{\eta_1}\right) = O\left(\frac{\Delta\rho g V^2}{\eta_1 R^4}\right). \tag{3.35}$$

Integrating this gives

$$R = O\left(\frac{\Delta\rho g V^2}{\eta_1} t\right)^{1/5}. \tag{3.36}$$

The full solution for (3.36) may be found by solving the governing equations

$$\partial_r p_2 = \eta_2 \partial_{zz} u_2, \tag{3.37}$$

and

$$\partial_z p_2 = -\Delta\rho g. \tag{3.38}$$

This problem is the same as that addressed by Lister & Kerr (1989). They solved for the plug flow of a neutrally buoyant gravity current spreading at a flat interface between two viscous fluids. They noted that plug flow occurs provided that λ is not too small, although they did not mention the upper limit ($\lambda \ll R/a$) on the current viscosity for which the solution applies. A similarity solution was found for the current thickness a in terms of r and t. The relation between the radial extent and time is

$$R = \left[\frac{125 V^2}{256\pi}\frac{\Delta\rho g}{\eta_1}\right]^{1/5} t^{1/5}. \tag{3.39}$$

The lubrication solution (3.39) is plotted in figure 8. The curves for the isoviscous drops and currents approach this solution. The $\lambda = 0.1$ drops and currents also approach this solution near the end of the computations. The spreading rate exponents for $\lambda = 1$ and 0.1 given in table 2 are close to the lubrication theory value of 1/5.

In order to see more clearly the approach of the numerical solutions to the asymptotic solutions, figure 10 shows $R/t^{1/5}$ for the slender body theory solution, the lubrication solution, and the $\lambda = 0$ and 0.1 numerical gravity currents. Figure 10 uses both the analytic SBT solution (3.33) found from setting $c_1 = 0$, and the solution to (3.32) if we assume that $c_1 = 0.8$. After normalizing by $t^{1/5}$, the $\lambda = 0$ current seems to increase logarithmically, while the $\lambda = 0.1$ one flattens and approaches the lubrication solution.

During early stages of spreading, it is possible to have drops with $\lambda \gg a/R[\ln(R/a)]^{-1}$ spread according to SBT, before reaching the asymptotic conditions for lubrication theory to apply. Initially the drops tend to have thick rims even though Δa is not small. The velocity resulting from force distributed along the rim of the drop is larger by a factor of $\ln R/a$ than the velocity resulting from an equal force distributed over the lower surface of the drop. This can be seen by comparing (3.10) and (3.35), the velocities which result from a stress of order $\Delta\rho g a$ distributed over the drop rim and over the lower surface respectively. Slender body theory will apply to any drop which has larger motion driven by the rim than from the lower surface. This may be the

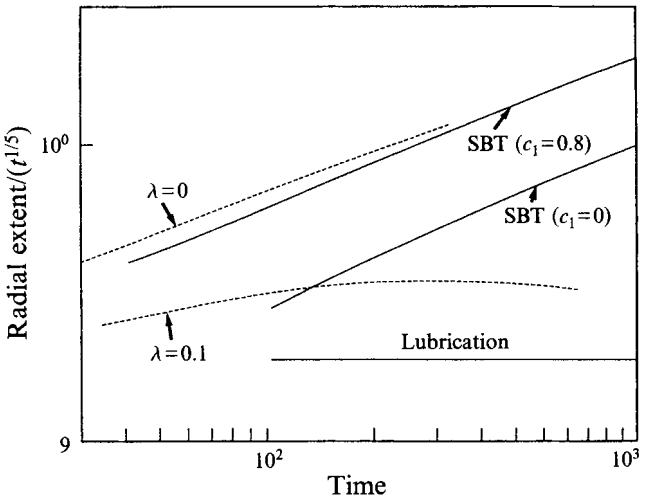

FIGURE 10. Log plot of $R/t^{1/5}$ versus t for the SBT solution with $c_1 = 0$, 0.8 (solid curves), and for the lubrication solution (solid straight line). These are compared with $R/t^{1/5}$ for the numerical gravity current solutions having $\lambda = 0$ and 0.1 (dashed).

reason that the $\lambda = 0.1$ currents and drops retained a lip near the rim similar to that observed for $\lambda = 0$ in figure 5.

We may also compare the theoretical results with Griffiths & Campbells' (1991) experimental observations. Since they used fluids with $\lambda \approx 10^{-3}$, the drops should spread according to slender body theory at large times. They measured the drop spreading and found the empirical relation

$$R = (1.3 \pm 0.1)t^{0.22\pm0.02}.$$

The coefficient 1.3 ± 0.1 agrees with our numerically derived coefficient for $\lambda = 0$, which is $b = 1.2$. The exponent here is slightly larger than the $t^{1/5}$ expected for lubrication, and might indeed be modelled better by the $[t \ln t]^{1/5}$ behaviour predicted by the slender body theory result.

Lister & Kerr (1989) considered the spread of gravity currents at a fluid interface with $\lambda \approx 1$ and also found that the spreading rate exponent exceeds the value of 1/5 predicted by lubrication theory (their figure 6). In this case the viscosity contrast indicates that it should spread according to lubrication theory. They suggested that the faster spreading may be caused by gradients in surface tension at the free surface. It is also possible that these currents still have fat rims, as indicated by their photos (e.g. their figure 8), so that large resistance at the rim causes slender body theory spreading behaviour.

3.3. *Viscous drops: the 'stiff' solution*

For a very viscous current, we may have larger radial variations than vertical variations, so that

$$\frac{U_2}{R^2} \gg \frac{\hat{u}_2}{a^2}. \tag{3.40}$$

The value of λ at which this applies is obtained from considering the tangential stress condition at the lower surface of the drop (3.12). Since $U_2 = O(u_\ell) \gg \hat{u}_2$, (3.12) indicates that (3.40) holds for $\lambda \gg R/a$.

The r-component of the equation of motion then has the scaling

$$\frac{p_2}{R} = O\left(\eta_2 \frac{U_2}{R^2}\right). \tag{3.41}$$

The z-component scaling (3.4) still applies, and we combine this with the scaling of continuity to get

$$p_2 = O(\eta_2 w_2/a) = O(\Delta\rho g a), \tag{3.42}$$

where the second equality in (3.42) is required to drive the motion.

Combination of (3.41) and (3.42) yields

$$\frac{\mathrm{d}R}{\mathrm{d}t} \equiv U_2 = O\left(\frac{\Delta\rho g a R}{\eta_2}\right). \tag{3.43}$$

Using the scaling from volume conservation and integrating, we obtain the result

$$R = O\left(\frac{\Delta\rho g V}{\eta_2} t\right)^{1/2}. \tag{3.44}$$

So for the case $\lambda \gg R/a$, $R \sim t^{1/2}$. From (3.44) we determine that for times greater than $t \ll a^2(\Delta\rho g V/\eta_2)^{-1}$, a viscous current will begin to approach lubrication theory.

Again we wish to justify the assumption that there is negligible pressure on the current from the fluid below Using (3.41), (3.13), and $U_2 = u_\ell$, we obtain

$$\frac{p_2}{p_\ell} = O\left(\lambda \frac{U_2/R}{u_\ell/R}\right) = O(\lambda) \gg R/a \gg 1 \tag{3.45}$$

so we can again assume that $p_2 = 0$ is the normal stress condition on the bottom of the current.

The quantitative solution corresponding to (3.44) is obtained by solving

$$\partial_z p = -\Delta\rho g + \eta_2 \partial_{zz} w. \tag{3.46}$$

and

$$\partial_r p = \eta_2 \partial_r \left[\frac{1}{r}\partial_r (ru)\right]. \tag{3.47}$$

We integrate (3.46), use the condition that the normal stress is zero on the lower surface of the drop $z = a$ to determine the integration constant, and use continuity to obtain

$$p = -\Delta\rho g(z - a) - 2\eta_2 \frac{1}{r}\partial_r (ru). \tag{3.48}$$

Substituting (3.48) into the r-momentum equation (3.47) gives

$$\frac{\Delta\rho g}{\eta_2}\partial_r a = 3\partial_r \left[\frac{1}{r}\partial_r (ru)\right]. \tag{3.49}$$

Combining the kinematic condition $w = \mathrm{D}a/\mathrm{D}t$ with the integration of continuity with respect to z yields

$$\partial_t a + a\frac{1}{r}\partial_r (ru) + u\partial_r a = 0. \tag{3.50}$$

From the scaling we expect the radial extent to depend on time according to the scaling in (3.44). So we look for a similarity solution by defining

$$r' = r/R, \qquad a' = aR^2/V, \qquad u' = u/\mathrm{d}R/\mathrm{d}t. \tag{3.51}$$

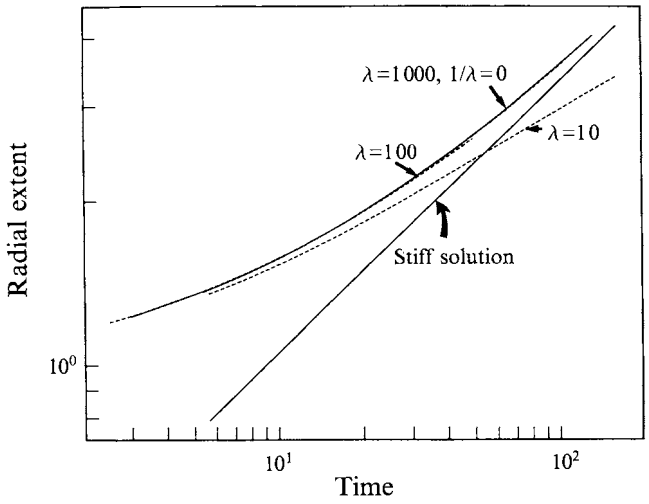

FIGURE 11. Log plot of R versus t comparing the stiff solution (solid) with the gravity current numerical results for $\lambda = 10$, 100, 1000 (dashed) and ∞ (solid). R is non-dimensionalized using R_0 and t using $\Delta\rho g R_0/\eta_2$.

Substituting (3.51) into (3.50), integrating, and using the condition that $u' = 1$ at $r' = 1$ gives (omitting primes)

$$u = r. \tag{3.52}$$

Substituting (3.51) into (3.49), and using (3.52) and the constant volume constraint (3.1), the drop thickness is found to be independent of the radial coordinate:

$$a = \frac{1}{\pi}. \tag{3.53}$$

A final condition is that the integral of the normal stress over the vertical coordinate at the rim of the drop must be zero, because the inviscid outer fluid does not resist the spreading. Making use of (3.52), k can be determined:

$$k^2 = \frac{1}{6\pi}.$$

Therefore the solution relating R and t is

$$R = \left(\frac{\Delta\rho g V}{6\pi\eta_2} t\right)^{1/2}. \tag{3.54}$$

This solution is plotted in figure 11 along with the numerical solutions for currents having $\lambda = 10$, 100, 1000 and ∞. These last three solutions are nearly identical. These are plotted on a different graph from the lower-viscosity asymptotic solutions, because the stiff solution and the $1/\lambda = 0$ current solution depend on the current viscosity η_2, while the lubrication and SBT solutions depend on η_1. Figure 11 indicates that the numerical solutions having very large λ approach the stiff solution.

The $\lambda = 10$ current starts in the 'stiff' category, and reaches $\lambda = R/a$ at about $R = 2$, at which point it approaches the lubrication solution. The very viscous $\lambda = 100$, 1000 and ∞ currents remain in the stiff current category for these calculations. The disk-like shape predicted by (3.53) is illustrated by the $\lambda = \infty$ current in figure 5.

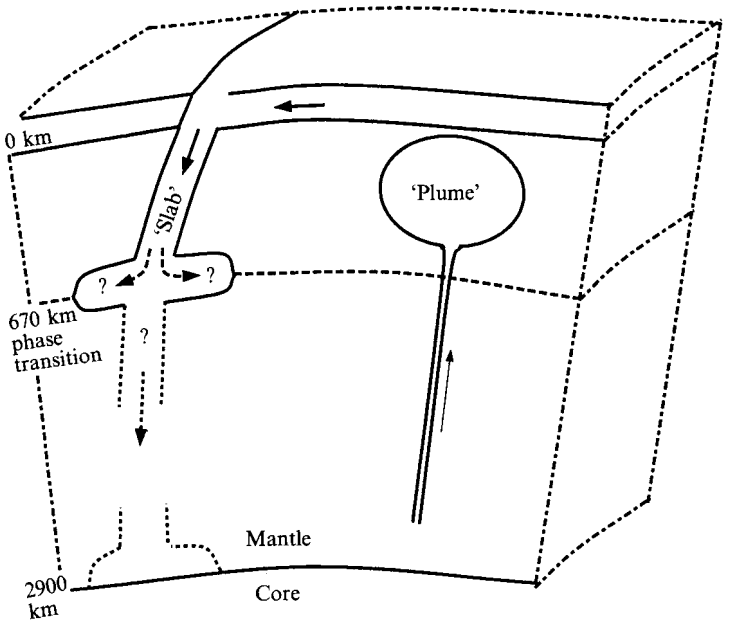

FIGURE 12. A cartoon showing a descending slab and ascending plume in the Earth's mantle. Slab material may spread laterally at the 670 km phase transition, and/or descend into the lower mantle and spread along the core–mantle boundary.

4. Application to mantle 'slab' currents

Solutions for the flow of highly viscous gravity currents can be applied to study the spreading behaviour of cold dense ocean plate material (or slabs) after it has sunk from the surface to a depth of neutral buoyancy in the mantle. Slabs coincide with the downwelling limbs of mantle convection, and have typical dimensions of about 100 km thickness and thousands of kilometres in length (see figure 12). At 670 km depth in the mantle, there is an increase in mantle density due to an endothermic phase transition and possibly a chemical change. There is ongoing debate about whether slabs are neutrally buoyant at this depth and spread laterally, or whether the slabs are able to penetrate the density discontinuity and sink further to the boundary between the mantle and the underlying dense liquid core. Since the phase change at 670 km is endothermic, the cold slab causes the discontinuity to be deflected downward, and this deflection exerts a restoring force which resists slab penetration. But eventually enough dense slab material accumulates that this load overcomes the restoring force and the slab material cascades into the lower mantle. Among recent studies which investigate this problem are three-dimensional numerical convection models by Machetel & Weber (1991), Tackley *et al.* (1993) and Honda *et al.* (1993). Although many two-dimensional convection models include temperature-dependent viscosity, these three-dimensional calculations do not. The slab–mantle viscosity contrast is not well known, and the range estimated by Griffiths & Turner (1988) is $40 < \lambda < 10^5$. Very high values should inhibit spreading along the discontinuity and lead to much more rapid vertical accumulation than is indicated by isoviscous models. We use gravity current solutions for a highly viscous slab to study the effect of viscosity on slab spreading, whether it occurs at 670 km or along the core–mantle boundary.

Two previous studies have used asymptotic gravity current theories to consider slab spreading at 670 km. Bercovici, Schubert & Tackley (1993) applied the solutions derived by Huppert (1982) for a two-dimensional planar and an axisymmetric gravity current spreading above a rigid surface to study how slab material would spread at the 670 km discontinuity. They used an axisymmetric current to model the polygonal corners of downwelling convective cells (i.e. where slabs intersect), and the planar current to model the edges of the convective cells. They concluded that an axisymmetric current is likely to exert sufficient force to penetrate the phase transition at 670 km, but the planar current would not. One problem with this study is the assumption that the mantle beneath the phase transition is viscous enough to be approximated by a rigid surface. It is possible that the mantle viscosity increases by as much as two orders of magnitude at this depth (e.g. Richards & Hager 1984), but the slab viscosity is likely to greatly exceed the viscosity of the lower mantle. In an earlier study, Kerr & Lister (1987) modelled slab spreading using asymptotic lubrication theory solutions for a gravity current at a fluid–fluid interface (Lister & Kerr 1989). As shown in § 3, the lubrication solutions are valid for an intermediate range of viscosity contrast between the current and the surrounding fluid layers ($a/R \ll \lambda \ll R/a$). However, slabs may be viscous enough to be better modelled using the stiff theory solutions, so we will compare the spreading predicted by stiff theory with that of lubrication theory.

We consider a modified version of the stiff gravity current theory derived in § 3. Because of the tabular shape of the slabs, we assume a two-dimensional planar current. And since slab material is added at a nearly constant rate we use a constant flux of material at the centre axis of the current.

The scaling of the governing equations is the same as for the stiff axisymmetric current, except that the volume constraint is now

$$\int_0^L a(x)\mathrm{d}x = Qt, \tag{4.1}$$

where L is the current length, a is the thickness, x is the horizontal coordinate, and Q is the flux.

The lubrication theory solution ($a/L \ll \lambda \ll L/a$) for this problem derived by Lister & Kerr (1989) is

$$L = 0.524 \left(\frac{\Delta\rho g Q^2}{\eta_1}\right)^{1/3} t. \tag{4.2}$$

For the stiff case, $\lambda \gg L/a$, following the procedure described in § 3, but using (4.1) instead of (3.1), we obtain the spreading relation

$$L = \frac{\Delta\rho g Q}{6\eta_2} t^2. \tag{4.3}$$

We compare the rate of spreading for these two cases, using typical mantle parameters. Using a slab subduction or sinking rate of 80 km My^{-1} gives a flux of about $Q = 3200$ km^2 My^{-1}. Slab–mantle density contrast and mantle viscosity are assumed to be $\Delta\rho = 100$ kg m^{-3} and $\eta_1 = 2 \times 10^{21}$ Pa s respectively. Using these values and (4.2), lubrication theory predicts that the slab material would spread at a rate of about

$$\frac{L}{t} \approx 30 \ \frac{\mathrm{km}}{\mathrm{My}}. \tag{4.4}$$

This rate is slightly lower than the subduction rate, so that material would tend to accumulate. Using the same parameters in (4.3), and assuming a value of $\lambda = 1000$, the stiff theory predicts a spreading rate of

$$\frac{L}{t} \approx 0.016\, t\, \frac{\text{km}}{\text{My}^2}. \tag{4.5}$$

The stiff slab current has a rate which begins much smaller than the lubrication slab, but increases with time. Using these rates, lubrication theory and stiff theory predict that it would take about 300 and 750 million years respectively for slab material to spread 1/4 the circumference of the 670 km discontinuity. Eventually the $\lambda = 1000$ slab would spread according to lubrication theory, but this would take about 2 billion years.

But we might ask whether slab stiffness would enable immediate penetration of the discontinuity. Bercovici *et al.* (1993) considered the ratio of the downward force of accumulating slab material to the restoring force associated with the deflected phase boundary. This ratio is given by

$$F_R = \frac{\rho^2 \alpha g a}{\gamma \Delta \rho} \tag{4.6}$$

where ρ is the upper mantle density, $\Delta\rho$ is the density increase at the discontinuity, α is thermal expansivity, and γ is the Clapyron slope of the phase transition. We assume the same values they used ($\rho = 4 \times 10^3$ kg m^{-3}, $\Delta\rho = 0.1$, $\gamma = 4$ MPa K^{-1}, $\alpha = 3 \times 10^{-5}$ K^{-1}), and get current thickness from (4.4) or (4.5) and conservation of volume scaling. Lubrication theory (4.4) (for a current at a fluid interface rather than at a solid surface as assumed by Bercovici *et al.* 1993) predicts that this ratio is about $F_R = 0.5$ so that the slab load is not sufficient to permit penetration of the discontinuity. Stiff theory, (4.5), gives a force balance of $F_R = 600t^{-1}$ My. Therefore a stiff slab would immediately penetrate the discontinuity.

Although our theory indicates that stiff slabs should immediately penetrate the 670 km discontinuity, an important inhibiting effect not included in our study is trench migration. As slabs sink into the mantle, very often the point of slab descent (the trench) moves laterally along the surface. As shown, for example, by experiments of Kincaid & Olson (1987), this migration significantly inhibits slab penetration of a density discontinuity. In gravity current theory, trench migration would reduce slab material accumulation as the source of the flux would move laterally at the rate of trench migration.

Assuming that slab material penetrates to the bottom of the mantle, the same theories apply for the spread of the slab material along the core–mantle boundary. It is generally believed that upwelling mantle plumes originate from a boundary layer at the core–mantle boundary, and that the chemistry of these plumes reflects the evolution of the chemistry of the descending slab material (e.g. Campbell & Griffiths 1992). Therefore a slab spreading according to lubrication theory would allow for relatively rapid assimilation of slab material into plume material, but stiff theory indicates that such assimilation would be considerably slower.

5. Conclusions

We have studied the way drops and gravity currents spread beneath a free surface, using the boundary integral method for initial spreading and asymptotic theories for very large spreading. A scaling analysis indicates that the spreading behaviour of gravity currents is described by three different relations, depending on the relative

Viscosity	$\lambda \ll a/R[\ln(R/a)]^{-1}$	$a/R \ll \lambda \ll R/a$	$\lambda \gg R/a$
Resistance	Rim	Lower surface	Within current
$R(t)$	$R = O\left(\left(\frac{\Delta\rho g V^2}{\eta_1} t \ln\left(\frac{\Delta\rho g R_0 t}{\eta_1}\right)\right)^{1/5}\right)$	$R = O\left(\left(\frac{\Delta\rho g V^2}{\eta_1} t\right)^{1/5}\right)$	$R = O\left(\left(\frac{\Delta\rho g V}{\eta_2} t\right)^{1/2}\right)$
Theory	Slender body	Lubrication	'Stiff'

TABLE 3. Scaling analysis summary for the three types of spreading behaviour

value of the viscosity contrast and the aspect ratio of the current. The results of the scaling analysis are summarized in table 3. The table shows where the greatest resistance to drop spreading occurs, the scaled dependence of radial extent R on time, and the theories described in §§ 3.1–3.3.

The fastest spreading occurs for very small viscosity contrast and is described by slender body theory. We derived the lowest-order solution, and higher-order terms should be obtained in future studies. The lubrication theory derived by Lister & Kerr (1989) applies for intermediate viscosity contrast. For very large viscosity contrast, we derived a stiff solution which predicts much slower spreading than applies for the lubrication theory or slender body theory solutions.

We were able to verify these asymptotic solutions with numerical solutions for gravity currents. The solution for $\lambda = 0$ approaches the slender body theory solution, and the $1/\lambda = 0$ solution approaches the stiff solution. At intermediate values, such as $\lambda = 1, 0.1$ and 10, the numerical results approach the lubrication solution. Experiments using drops with small λ seem to spread faster than is indicated by lubrication theory, and this may be because they are better described by slender body theory.

We applied a variation of the stiff solution to consider the way slabs spread at depths of neutral buoyancy in the Earth's mantle. We conclude that if the slabs are viscous enough to be described by stiff theory, it is highly unlikely that the phase transition at 670 km would stop slabs from sinking deeper into the mantle. However if the trench, the point where slabs descend into the mantle, migrates laterally, slab penetration at 670 km may be inhibited. Otherwise it is likely that stiff slabs would sink to the bottom of the mantle and spread slowly along the core–mantle boundary. But if the slab–mantle viscosity contrast is small enough to be described by lubrication theory, it is quite likely that slab material sinks to the 670 km phase transition and spreads laterally, never accumulating enough mass to sink further.

We are grateful to Neil Ribe, Howard Stone, Edward Bolton, Ronald Smith, Michael Manga and three anonymous reviewers for helpful discussions and comments on the manuscript. We also thank Howard Stone for providing a copy of his boundary integral code, for numerical advice, and for showing us how to simplify the SBT derivation by using elliptic integrals. The research was supported by NSF grant EAR-89-16241.

REFERENCES

ASCOLI, E. P., DANDY, D. S. & LEAL, L. G. 1990 Buoyancy-driven motion of a deformable drop toward a planar wall at low Reynolds number. *J. Fluid Mech.* **213**, 287–311.

BATCHELOR, G. K. 1970 Slender-body theory for particles of arbitrary cross-section in Stokes flow. *J. Fluid Mech.* **44**, 419–440.

BERCOVICI, D., SCHUBERT, G. & TACKLEY, P. J. 1993 On the penetration of the 660 km phase change by mantle downflows. *Geophys. Res. Lett.* **20**, 2599–2602.

CAMPBELL, I. H. & GRIFFITHS, R. W. 1992 The changing nature of mantle hotspots through time: Implications for the chemical evolution of the mantle. *J. Geology* **92**, 497–523.

CANRIGHT, D. R. 1987 A finite-amplitude analysis of the buoyant instability of a highly viscous film over a less viscous half-space. PhD thesis, University of California, Berkeley.

CHI, B. K. & LEAL, L. G. 1989 A theoretical study of the motion of a viscous drop toward a fluid interface at low Reynolds number. *J. Fluid Mech.* **201**, 123–146.

DAVIS, R. H., SCHONBERG, J. A. & RALLISON, J. M. 1989 The lubrication force between two viscous drops. *Phys. Fluids* A **1**, 77–81.

GELLER, A. S., LEE, S. H. & LEAL, L. G. 1986 The creeping motion of a spherical partical normal to a deformable interface. *J. Fluid Mech.* **169**, 27–69.

GRIFFITHS, R. W. & CAMPBELL, I. H. 1990 Stirring and structure in mantle starting plumes. *Earth Planet. Sci. Lett.* **99**, 66–78.

GRIFFITHS, R. W. & CAMPBELL, I. H. 1991 Interaction of mantle plume heads with the Earth's surface and onset of small-scale convection. *J. Geophys. Res.* **96**, 18295–18310.

GRIFFITHS, R. W. & TURNER, J. S. 1988 Folding of viscous plumes impinging on a density or viscosity interface. *Geophys. J.* **95**, 397–419.

HONDA, S., BALACHANDAR, S., YUEN, D. A. & REUTELER, D. 1993 Three-dimensional mantle dynamics with an endothermic phase transition. *Geophys. Res. Lett.* **20**, 221–224.

HUPPERT, H. E. 1982 The propagation of two-dimensional and axisymmetric viscous gravity currents over a rigid horizontal surface. *J. Fluid Mech.* **121**, 43–58.

KERR, R. C. & LISTER, J. R. 1987 The spread of subducted lithospheric material along the mid-mantle boundary. *Earth Planet. Sci. Lett.* **85**, 241–247.

KINCAID, C. & OLSON, P. 1987 An experimental study of subduction and slab migration. *J. Geophys. Res.* **92**, 13832–13840.

KOCH, D. M. 1993 A spreading drop model for plumes on Venus. PhD thesis, Yale University.

KOCH, D. M. 1994 A spreading drop model for mantle plumes and volcanic features on Venus. *J. Geophys. Res.* **99**, 2035–2052.

KOCH, D. M. & RIBE, N. M. 1989 The effect of lateral viscosity variations on surface observables. *Geophys. Res. Lett.* **16**, 535–538.

KOH, C. J. & LEAL, L. G. 1989 The stability of drop shapes for translation at zero Reynolds number through a quiescent fluid. *Phys. Fluids* A **8**, 1309–1313.

KOJIMA, M., HINCH, E. J. & ACRIVOS, A. 1984 The formation and expansion of a toroidal drop moving in a viscous fluid. *Phys. Fluids* A **27**, 19–32.

LEE, S. H. & LEAL, L. G. 1982 The motion of a sphere in the presence of a deformable interface. *J. Fluid Mech.* **87**, 81–106.

LISTER, J. R. & KERR, R. C. 1989 The propagation of two-dimensional and axisymmetric viscous gravity currents at a fluid interface. *J. Fluid Mech.* **203**, 215–249.

MACHETEL, P. & WEBER, P. 1991 Intermittent layered convection in a model with an endothermic phase change at 670 km. *Nature* **350**, 55–57.

MANGA, M., STONE, H. A. & O'CONNELL, R. J. 1993 The interaction of plume heads with compositional discontinuities in the Earth's mantle. *J. Geophys. Res.* **98**, 19979–19990.

POZRIKIDIS, C. 1990*a* The instability of a moving viscous drop. *J. Fluid Mech.* **210**, 1–21.

POZRIKIDIS, C. 1990*b* The deformation of a liquid drop moving normal to a plane wall. *J. Fluid Mech.* **215**, 331–363.

RALLISON, J. M. & ACRIVOS, A. 1978 A numerical study of the deformation and burst of a viscous drop in an extensional flow. *J. Fluid Mech.* **1978**, 191–200.

RICHARDS, M. A. & HAGER, B. H. 1984 Geoid anomalies in a dynamic earth. *J. Geophys. Res.* **89**, 5987–6002.

STONE, H. A. & LEAL, L. G. 1989 Relaxation and breakup of an initially extended drop in an otherwise quiescent fluid. *J. Fluid Mech.* **198**, 399–427.

TACKLEY, P. J., STEVENSON, D. J., GLATZMAIER, G. A. & SCHUBERT, G. 1993 Effects of an endothermic phase transition at 670 km depth in a spherical model of convection in the Earth's mantle. *Nature* **361**, 699–704.

TANZOSH, J., MANGA, M. & STONE, H. A. 1992 Boundary integral methods for viscous free-boundary problems: Deformation of single and multiple fluid-fluid interfaces. In *Boundary Element Technology VI* (ed. C. A. Brebbia & M. S. Ingber), pp. 19–39. Elsevier Applied Science.

WHITEHEAD, J. A. & LUTHER, D. S. 1975 Dynamics of laboratory diapir and plume models. *J. Geophys. Res.* **80**, 705–717.

YIANTSIOS, S. G. & DAVIS, R. H. 1990 On the buoyancy-driven motion of a drop towards a rigid surface or a deformable interface. *J. Fluid Mech.* **217**, 547–573.